Interpolated boundary condition for lattice Boltzmann simulations of flows in narrow gaps

B. Chun and A. J. C. Ladd*

Department of Chemical Engineering, University of Florida, Gainesville, Florida 32611, USA
(Received 21 December 2006; published 26 June 2007)

Several different interpolation schemes have been proposed for improving the accuracy of lattice Boltzmann simulations in the vicinity of a solid boundary. However, these methods require at least two or three fluid nodes between nearby solid surfaces, a condition that may not be fulfilled in dense suspensions or porous media for example. Here we propose an interpolation of the equilibrium distribution, which leads to a velocity field that is both second-order accurate in space and independent of viscosity. The equilibrium interpolation rule infers population densities on the boundary itself to reduce the span of nodes needed for interpolation; it requires a minimum of one grid spacing between the nodes. By contrast, the linear interpolation rule requires two fluid nodes in the gap and leads to a viscosity-dependent slip velocity, while the multireflection rule is viscosity independent but requires a minimum of three fluid nodes.

I. INTRODUCTION

Over the past ten years, the lattice Boltzmann equation (LBE) has emerged as the basis of important numerical methods to study flows in complex geometries. Applications include flows in porous media [1–3], particle suspensions [4–7], polymer solutions [8,9], and microfluidic devices [10,11]. The key issue in such computations is an accurate and computationally efficient implementation of the no-slip boundary condition between solid and fluid surfaces. The most common boundary condition in LBE simulations is the bounce-back rule, which can be straightforwardly modified for the case of a moving solid surface [12]. The no-slip boundary is located approximately half-way between the solid and fluid nodes [13], but the exact position depends on the orientation of the solid surface with respect to the underlying lattice and the fluid viscosity [14]. There have been many proposals to improve the accuracy of the solid-fluid boundary condition. Initially, effort focused on solving equations for the distribution function at fluid nodes adjacent to the solid surface [15–20]. However, these methods were found to be overly complicated in the general case and have not been widely utilized. An alternative idea is to establish the boundary condition on the links between the nodes; this was first described within the context of lattice-gas models of suspensions [21], and was later adapted to lattice Boltzmann models [12,15]. However, the link bounce-back rule leads to a hydrodynamic boundary that is offset from the physical one, and several link-based interpolation schemes have been proposed to obtain a more accurate no-slip condition [22–28].

A simple, physically motivated interpolation scheme has been proposed [26,29], which both improves the accuracy of the bounce-back rule and is unconditionally stable for all boundary positions; the scheme has both linear and quadratic versions. A more general framework for this class of interpolation schemes has been extensively analyzed in a comprehensive and seminal paper [30]. The multireflection rule proposed in Ref. [30] is the most accurate boundary condition yet discovered for lattice Boltzmann methods. However, interpolation requires additional fluid nodes in the gap between adjacent particle surfaces. The bounce-back rule requires only one grid spacing between the surfaces, but linear interpolation requires at least two grid spacings, while quadratic interpolation and multireflection require three. In this work we consider interpolation of the equilibrium distribution only. Although this is more complex to implement than linear interpolation, it has the advantage that the velocity distribution at the boundary surface may be used to provide an additional interpolation point. In this way the span of fluid nodes can be reduced to that of the bounce-back rule, while obtaining second-order accuracy in the flow field. In conjunction with an appropriate choice of collision operator [30], the location of the boundary is independent of fluid viscosity, unlike the linear and quadratic interpolations. For viscous fluids, where the relaxation time $\tau > 1$, the equilibrium interpolation rule is significantly more accurate than either linear or quadratic interpolation.

We have compared results obtained using the equilibrium interpolation rule with three different interpolation schemes: linear, quadratic [26], and multireflection [30]. We use a version [31] of the multiple-relaxation time (MRT) lattice Boltzmann model [32], which is tuned to minimize the dependence of the boundary location on the fluid viscosity [30]. We have examined flows in channels oriented at different angles with respect to the underlying grid and flows through porous media composed of regular arrays of spheres. Our work parallels that reported in Ref. [3], with the addition of the equilibrium interpolation rule.

II. MULTIPLE-RELAXATION-TIME (MRT) MODEL

The time evolution of the distribution function in discrete phase space is described by the lattice Boltzmann equation. If $n_i(\mathbf{r}, t)$ represents the density of particles moving in the direction labeled i at the discrete location $\mathbf{r}$ and discrete time t, then

*ladd@che.ufl.edu

TABLE I. Eigenvectors and eigenvalues of the D3Q19 collision operator [37]. The M10 model [12,40] uses separate bulk and shear viscosities, while the two-relaxation-time (TRT) model [30] uses separate values for the odd and even modes.

	Weighted [31]	Unweighted [32]	TRT	M10	BGK
0	1	1	0	0	0
1	c_x	c_x	0	0	0
2	c_y	c_y	0	0	0
3	c_z	c_z	0	0	0
4	c^2-1	$19c^2-30$	λ	λ_v	λ
5	$3c_x^2-c^2$	$3c_x^2-c^2$	λ	λ	λ
6	$c_y^2-c_z^2$	$c_y^2-c_z^2$	λ	λ	λ
7	$c_y c_z$	$c_y c_z$	λ	λ	λ
8	$c_z c_x$	$c_z c_x$	λ	λ	λ
9	$c_x c_y$	$c_x c_y$	λ	λ	λ
10	$(3c^2-5)c_x$	$(5c^2-9)c_x$	λ'	-1	λ
11	$(3c^2-5)c_y$	$(5c^2-9)c_y$	λ'	-1	λ
12	$(3c^2-5)c_z$	$(5c^2-9)c_z$	λ'	-1	λ
13	$(c_y^2-c_z^2)c_x$	$(c_y^2-c_z^2)c_x$	λ'	-1	λ
14	$(c_z^2-c_x^2)c_y$	$(c_z^2-c_x^2)c_y$	λ'	-1	λ
15	$(c_x^2-c_y^2)c_z$	$(c_x^2-c_y^2)c_z$	λ'	-1	λ
16	$3c^4-6c^2+1$	$(21c^4-53c^2+24)/2$	λ	-1	λ
17	$(2c^2-3)(3c_x^2-c^2)$	$(3c^2-5)(3c_x^2-c^2)$	λ	-1	λ
18	$(2c^2-3)(c_y^2-c_z^2)$	$(3c^2-5)(c_y^2-c_z^2)$	λ	-1	λ

$$n_i(\mathbf{r}+\mathbf{c}_i\Delta t, t+\Delta t) = n_i(\mathbf{r},t) + \sum_{j=0}^{b}\mathcal{L}_{ij}n_j^{neq}(\mathbf{r},t) + f_i(\mathbf{r},t),$$

(1)

where $\mathcal{L}_{ij}$ is the linearized collision operator [33,34], $n_j^{neq} = n_j - n_j^{eq}$ is the nonequilibrium distribution function, and the lattice vectors are labeled by $i=0,1,\ldots,b$. The term f_i incorporates the effect of an external body force density, $\mathbf{f}$, such as gravity. In this work we will consider only Stokes flow, so that the equilibrium distribution is linear,

$$n_i^{eq} = a^{c_i}\rho\left[1 + \frac{\mathbf{u}\cdot\mathbf{c}_i}{c_s^2}\right],$$

(2)

and the forcing is simply $f_i = \mathbf{f}\cdot\mathbf{c}_i\Delta t/c_s^2$ [35]. The weighting factors, a^{c_i}, for the 19 velocity three-dimensional D3Q19 model are $a^0=1/3$, $a^1=1/18$, and $a^{\sqrt{2}}=1/36$. The sound speed is then given by $c_s^2=c^2/3$, where $c=\Delta/\Delta t$. Typically, we choose units such that the lattice grid spacing Δ and the time step Δt are equal to one. The fluid velocity is evaluated at the half time step by introducing the modified momentum $\mathbf{j}'=\mathbf{j}+\mathbf{f}\Delta t/2$ [12]. The improvement in accuracy from introducing this correction is described in [35].

The single relaxation time or Bhatnagar-Gross-Krook model (LBGK) has been the most popular collision operator, due to its computational simplicity [36,37]. However, the LBGK model suffers from numerical instability and inaccuracy near boundaries when compared with the MRT model [3,38,39], which relaxes the nonhydrodynamic modes at a

different rate from the viscous modes. The modes or moments of the distribution function can be constructed from appropriate linear combinations,

$$m_k = \sum_{j=0}^{b} e_{k,j}n_j,$$

(3)

where $\mathbf{e}_k$ is the kth eigenvector of the collision operator $\mathcal{L}$. These eigenvectors can be constructed from irreducible polynomials of the lattice-vectors $\mathbf{c}_i$ [32], and are listed in Table I. The first four moments correspond to the conserved variables, mass density ρ and momentum density $\mathbf{j}$, while m_4-m_9 are related to the bulk and shear stresses. The higher modes, $m_{10}-m_{18}$, are kinetic or "ghost" modes; they do not enter the bulk hydrodynamic equations, but play an important role near boundaries [30] and when there are thermal fluctuations [31].

There are two slightly different sets of eigenvectors shown in Table I. In the original formulation of the MRT model [32], the back transformation,

$$n_i = \sum_{k=0}^{b} w_k^{-1}m_k e_{k,i}, \quad w_k = \sum_{i=0}^{b} e_{k,i}^2,$$

(4)

is simply the inverse of the forward transformation, with w_k the normalizing factor of the kth eigenvector. The eigenvectors must therefore satisfy the orthogonality relation

$$\sum_{k=0}^{b} w_k^{-1} e_{k,i} e_{k,j} = \delta_{ij}. \tag{5}$$

However, a drawback of this choice of eigenvectors is that the equilibrium distribution has projections onto the kinetic modes [32]. An alternative set of eigenvectors can be constructed so that the back transformation includes the weights from the equilibrium distribution [31],

$$n_i = \sum_{k=0}^{b} a^{c_i} w_k^{-1} m_k e_{k,i}, \quad w_k = \sum_{i=0}^{b} a^{c_i} e_{k,i}^2. \tag{6}$$

These eigenvectors satisfy a slightly different orthogonality condition,

$$\sum_{k=0}^{b} a^{c_i} w_k^{-1} e_{k,i} e_{k,j} = \delta_{ij}, \tag{7}$$

and the equilibrium distribution now has no projection onto the kinetic modes. The decoupling of the equilibrium distribution from the kinetic modes significantly simplifies the implementation of thermal fluctuations [31]. Moreover, the MRT model with weighted eigenvectors reduces to the LBGK [37] and ten-moment [12,40] models by a suitable choice of eigenvalues. We have found that collision operators constructed from either set of eigenvectors show similar numerical stability and tunability.

The MRT model can be updated with about a 20% computational overhead over the LGBK model. The moments of the distribution m_k are first calculated from Eq. (3), and then relaxed towards their local equilibrium,

$$m_k^* = m_k^{eq} + (1 + \lambda_k)(m_k - m_k^{eq}). \tag{8}$$

The asterisk indicates the postcollision state, λ_k is the eigenvalue of the kth mode, and the equilibrium moments are calculated from the analog of Eq. (3),

$$m_k^{eq} = \sum_{j=0}^{b} e_{k,j} n_j^{eq}. \tag{9}$$

The eigenvalues of the conserved modes (m_0-m_3) are necessarily zero, and the equilibrium moments are therefore unchanged by the collision process. Using the weighted eigenvectors from Table I, we find that the equilibrium distribution only has a projection onto the hydrodynamic and viscous modes (m_0-m_9), while the linearized equilibrium distribution [Eq. (2)] has no projection on the viscous modes either and Eq. (8) simplifies to

$$m_k^* = (1 + \lambda_k) m_k. \tag{10}$$

The postcollision distribution, n_i^*, can be calculated from Eq. (6) and then propagated according to Eq. (1),

$$n_i(\mathbf{r} + \mathbf{c}_i \Delta t, t + \Delta t) = n_i^*(\mathbf{r}, t). \tag{11}$$

Symmetry considerations suggest a total of six distinct nonzero eigenvalues for the D3Q19 model; the bulk mode (m_4), the shear modes (m_5-m_9), two sets of third-order modes ($m_{10}-m_{12}$ and $m_{13}-m_{15}$), and two sets of fourth-order modes (m_{16} and $m_{17}-m_{18}$). However, in this work we will use one eigenvalue for the second-order and fourth-order modes, and a separate eigenvalue for the third-order modes. This allows for a straightforward tuning of the MRT model that can result in a viscosity-independent boundary condition for the bounce-back boundary condition [30] (see Sec. III B). Neither linear nor quadratic interpolations are viscosity independent [3], but the equilibrium interpolation scheme proposed here can be made viscosity independent in a similar way to the bounce-back rule. The multireflection boundary condition is independent of viscosity without any need for tuning of the collision operator [30].

III. SOLID-FLUID BOUNDARY

Boundary conditions in the lattice-Boltzmann method are derived from localized rules applied to the velocity distribution, as opposed to direct conditions on the velocity field. The additional physical insight provided by the underlying mechanics has been useful in the development of interpolation methods [26] as well as in the development of the moving boundary condition [21]. Before discussing specific boundary rules, we will clarify some definitions related to the various types of nodes on the grid. Solid nodes are the set of nodes overlaid by solid objects; all remaining nodes are fluid nodes. Boundary nodes are fluid nodes that share a link with a solid node, and neighboring nodes are fluid nodes adjacent to boundary nodes. In this work we focus on the no-slip boundary condition at stationary solid surfaces, while moving boundary conditions can be found elsewhere in the literature [12,21,29,30].

A. Link bounce-back boundary condition

In the link bounce-back rule [15,21], the boundary surface is assumed to lie midway between a boundary node and a solid node. A fluid population leaving the boundary node $\mathbf{r}_j$ and encountering the solid surface is reflected and returns in one time step to its original location, pointing in the opposite direction. The corresponding equation can be expressed as

$$n_{i'}(\mathbf{r}_j, t + \Delta t) = n_i^*(\mathbf{r}_j, t), \tag{12}$$

where n_i^* denotes the postcollision population, and the direction i' is opposite to i; i.e., $\mathbf{c}_{i'} = -\mathbf{c}_i$.

B. Tuning the MRT model

The relaxation time of a particular mode [Eq. (10)] can be related to its eigenvalue via a discrete fluctuation-dissipation theorem [12,31,35,41],

$$2\tau_k = \sum_{n=-\infty}^{\infty} (1 + \lambda_k)^{|n|} = -\frac{2}{\lambda_k} - 1. \tag{13}$$

The τ_k in Eq. (13) differs from the LBGK definition, $\tau = -1/\lambda$, by a constant offset of $-1/2$. In this work we will use a two-relaxation-time (TRT) model [30], with separate eigenvalues, λ and λ', for the even (m_4-m_9 and $m_{16}-m_{18}$) and odd ($m_{10}-m_{15}$) modes. The shear viscosity of the fluid is given by $\eta = \rho c_s^2 \tau$, where τ is given by Eq. (13). The merit of the TRT model is that the eigenvalues of the third-order modes

$(m_{10}-m_{15})$ can be tuned to adjust the location of the hydrodynamic boundary with respect to the underlying grid. Thus for a given τ we can adjust τ' to keep the location of the boundary independent of τ. We adopt the same tuning of the collision operator as in Ref. [30],

$$\lambda' = -\frac{2\tau}{\tau+w}, \qquad (14)$$

where the restriction $w>0$ is necessary for linear stability. For planar boundaries located midway between the grid points, the hydrodynamic boundary is located on the physical boundary when $w=3/8$, independent of fluid viscosity [30]. We have verified this relation for the weighted eigenvectors (Table II) as well.

Linear stability restricts the range of eigenvalues $-2 < \lambda_k < 0$ [34,42], but there is a more subtle limitation on the tunability of the boundary location. For fixed Reynolds number and grid resolution, the incompressible limit is reached by reducing the fluid viscosity so that $\tau \to 0$. To maintain the same position of the boundary $\tau'=w/2\tau$ becomes large, and the ratio $\tau'/\tau=w/2\tau^2$ eventually diverges. It has been shown that this introduces a compressibility error whenever this ratio becomes large in comparison to the number of grid points per linear dimension [43].

C. Interpolation

In general, the solid surface is not always located midway between the boundary node and the solid node; a second-order boundary condition therefore requires interpolation. The scheme proposed in Ref. [26] combines second-order accuracy with simplicity and stability. It uses different algorithms depending on the location of the boundary, in order to ensure that the distribution is always interpolated and never extrapolated; this ensures stability. The idea is illustrated in Fig. 1. If the surface is closer to the boundary node than the solid node ($q<1/2$), an interpolated population is constructed farther away from the surface and then bounced back to end up on the boundary node during the propagation step. Alternatively, if the solid surface is located closer to the solid node ($q>1/2$) the boundary-node population is bounced back to end up at an intermediate location during the propagation step. Then this intermediate distribution is combined with the neighboring population to interpolate to the boundary node. The equations for linear interpolation are

$$n_{i'}(\mathbf{r}_j, t+\Delta t) = 2q n_i^*(\mathbf{r}_j, t) + (1-2q) n_i^*(\mathbf{r}_j - \mathbf{c}_i, t),$$

$$n_{i'}(\mathbf{r}_j, t+\Delta t) = \frac{1}{2q} n_i^*(\mathbf{r}_j, t) + \frac{2q-1}{2q} n_{i'}^*(\mathbf{r}_j, t), \qquad (15)$$

for $0 \leq q < 1/2$ and $1/2 \leq q < 1$, respectively.

A quadratic interpolation [26] can be derived in a similar fashion, using an additional neighboring node at $\mathbf{r}_j - 2\mathbf{c}_i$ [48];

$$n_{i'}(\mathbf{r}_j, t+\Delta t) = q(2q+1) n_i^*(\mathbf{r}_j, t) + (1-4q^2) n_i^*(\mathbf{r}_j - \mathbf{c}_i, t)$$
$$- q(1-2q) n_i^*(\mathbf{r}_j - 2\mathbf{c}_i, t),$$

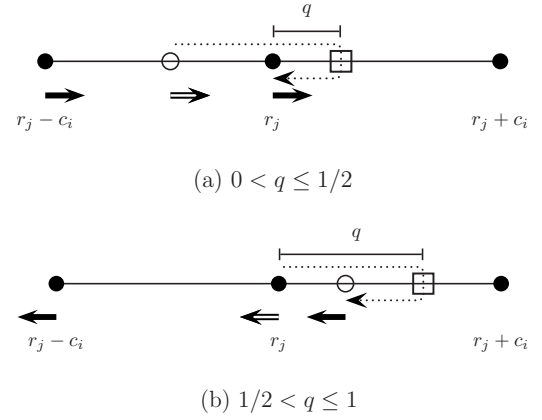
(a) $0 < q \leq 1/2$

(b) $1/2 < q \leq 1$

FIG. 1. Schematic diagrams of the linear interpolation rule [26]; r_j is a boundary node, r_j+c_i is a solid node, and r_j-c_i is a neighboring node; i is the direction towards the solid node. An open circle represents the location of an interpolated population and an open square indicates the position of the solid surface; q is the distance of the fluid node from the boundary surface, normalized by the grid spacing Δ. The double-line arrow represents the interpolated distribution obtained from two known distributions, which are denoted by single-line arrows.

$$n_{i'}(\mathbf{r}_j, t+\Delta t) = \frac{1}{q(2q+1)} n_i^*(\mathbf{r}_j, t) + \frac{2q-1}{q} n_{i'}^*(\mathbf{r}_j, t)$$
$$+ \frac{1-2q}{1+2q} n_{i'}^*(\mathbf{r}_j - \mathbf{c}_i, t). \qquad (16)$$

Although linear and quadratic interpolation schemes both lead to second-order accuracy at the boundaries, the location now depends on viscosity in a way that cannot be easily eliminated as it was for the bounce-back rule. The multireflection rule uses more general relations to construct a boundary condition that is viscosity independent [30]. The equations were derived from the Chapman-Enskog expansion at a planar boundary and use a total of three fluid nodes and five different populations:

$$n_{i'}(\mathbf{r}_j, t+\Delta t) = n_i^*(\mathbf{r}_j, t) + \frac{1-2q-2q^2}{(1+q)^2} n_i^*(\mathbf{r}_j - \mathbf{c}_i, t)$$
$$+ \frac{q^2}{(1+q)^2} n_i^*(\mathbf{r}_j - 2\mathbf{c}_i, t)$$
$$- \frac{1-2q-2q^2}{(1+q)^2} n_{i'}^*(\mathbf{r}_j, t)$$
$$- \frac{q^2}{(1+q)^2} n_{i'}^*(\mathbf{r}_j - \mathbf{c}_i, t). \qquad (17)$$

D. Interpolation of the equilibrium distribution

In many applications, the distance between solid boundaries may on occasion be comparable to the grid size, with insufficient fluid nodes in the gap for the desired interpolation scheme. In such situations a lower-order boundary condition is used, typically bounce back, but this can lead to

increased global errors, even when only a few nodes are affected [20]. Our proposed boundary condition is based on the observation that the nonequilibrium distribution is one order higher in the Chapman-Enskog expansion than the equilibrium distribution. Thus a first-order accurate nonequilibrium distribution, coupled with a second-order accurate equilibrium distribution, will result in an overall second-order distribution. Another way to say this is that the nonequilibrium distribution contributes terms of order $\nabla\mathbf{u}$ to the macrodynamical equations, and a first-order calculation of the velocity gradient is sufficient for a second-order velocity field. The computational advantage of this decomposition is that we can infer an equilibrium distribution at the solid surface to provide an additional interpolation point and compute an overall second-order distribution in situations where linear interpolation is not possible. An additional advantage is that any viscosity dependence of the hydrodynamic boundary comes from the nonequilibrium distribution. By interpolating just the equilibrium distribution, we can still tune the MRT model to provide a viscosity-independent boundary rule, as described in Sec. III B.

The distribution function at a boundary node is therefore divided into equilibrium and nonequilibrium parts, based on the local density and fluid velocity. The decomposition must be done before the distribution is propagated, so the equilibrium distribution is always interpolated first and then bounced back to the boundary node. To maintain stability we use different neighboring distributions to interpolate with, as illustrated in Fig. 2. When the surface is closer to the boundary node than the solid node ($q < 1/2$), we use the neighboring node at $\mathbf{r}_j - \mathbf{c}_i$ for the interpolation [Fig. 2(a)], as with the standard linear interpolation [c.f., Eq. (15)],

$$n_{i'}^{eq}(\mathbf{r}_j, t + \Delta t) = 2q n_i^{eq}(\mathbf{r}_j, t) + (1 - 2q) n_i^{eq}(\mathbf{r}_j - \mathbf{c}_i, t). \quad (18)$$

On the other hand, when the surface is closer to the solid node, we use the expected equilibrium distribution at the solid surface [Fig. 2(b)]:

$$n_{i'}^{eq}(\mathbf{r}_j, t + \Delta t) = \frac{1 - q}{q} n_i^{eq}(\mathbf{r}_j, t) + \frac{2q - 1}{q} n_i^{eq}(\mathbf{r}_b), \quad (19)$$

where $n_i^{eq}(\mathbf{r}_b) \equiv n_i^{eq}(\rho_b, \mathbf{u}_b)$ is the equilibrium distribution corresponding to the local velocity of the surface $\mathbf{u}_b$. The mass density at the surface, ρ_b, can be taken as the local fluid density $\rho(\mathbf{r}_j)$ or as the mean fluid density ρ_0. The difference is small, of the order of M^2, where M is the Mach number, and in Stokes flow M can be made arbitrarily small. Our simulations use a stationary surface, so in this case $n_i^{eq}(\mathbf{r}_b) = a^{c_i} \rho_0$. The final distribution at the boundary node, $n_{i'}(\mathbf{r}_j, t + \Delta t)$, includes the nonequilibrium distribution, which is obtained from the bounce-back rule,

$$n_{i'}^{neq}(\mathbf{r}_j, t + \Delta t) = n_i^{neq}(\mathbf{r}_j, t), \quad (20)$$

regardless of q.

When two surfaces are very close together, there may be no fluid node at $\mathbf{r}_j - \mathbf{c}_i$, as illustrated in Fig. 2(c). In the case when $q < 1/2$, we can use the equilibrium distribution at the other surface to interpolate with,
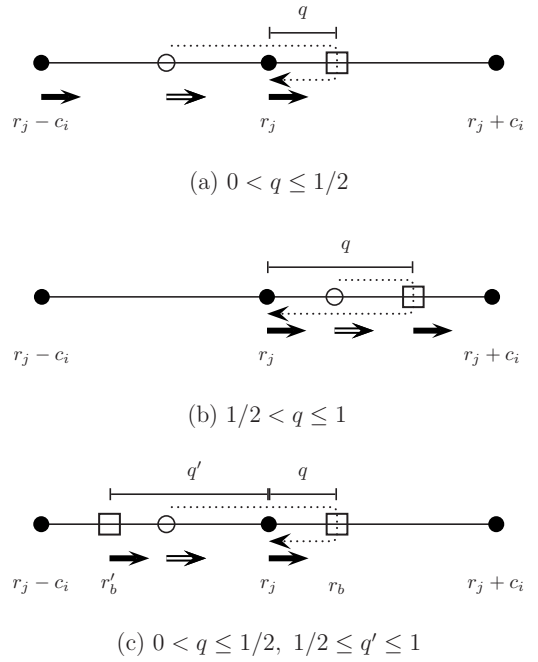

(a) $0 < q \leq 1/2$

(b) $1/2 < q \leq 1$

(c) $0 < q \leq 1/2$, $1/2 \leq q' \leq 1$

FIG. 2. Schematic diagrams of the equilibrium interpolation rule; r_j is a boundary node, $r_j + c_i$ is a solid node, and $r_j - c_i$ is a neighboring node in (a) and (b), but a solid node in (c); i is the direction towards the solid node. An open circle represents the location of an interpolated equilibrium population and an open square indicates the position of the solid surface; q is the distance of the fluid node from the boundary surface, normalized by the grid spacing Δ. The double-line arrow represents the interpolated distribution obtained from two known distributions, which are denoted by single-line arrows.

$$n_{i'}^{eq}(\mathbf{r}_j, t + \Delta t) = \frac{q' + 2q - 1}{q'} n_i^{eq}(\mathbf{r}_j, t) + \frac{1 - 2q}{q'} n_i^{eq}(\mathbf{r}_b'), \quad (21)$$

whereas when $q > 1/2$ we use Eq. (19). Equation (21) is stable when $q' > 1 - 2q$ and $q < 1/2$; otherwise the interpolated distribution becomes an extrapolated one. Thus the equilibrium interpolation rule requires only a single fluid node to provide second-order accuracy, and can replace the bounce-back rule whenever the gap between the solid surfaces is larger than Δ.

IV. RESULTS AND DISCUSSION

In order to assess the accuracy of the proposed equilibrium interpolation (EI) rule, we compare with other forms of interpolation; bounce back (BB), linear interpolation (LI), quadratic interpolation (QI), and multireflection (MR). The MRT collision rules were tuned according to Eq. (14), and results for flows in inclined channels and flows through idealized porous media are reported for different values of the tuning parameter w.

A. Plane Poiseuille flows

We consider first a planar Poiseuille flow in channels inclined at 0° and 45° to a grid line. Consider a planar channel

TABLE II. The slip velocity parameter, α, in 0° and 45° channels; the normalized slip velocity $\Delta u/u_{max}=4\alpha\Delta^2/L^2$. Results are shown for five different interpolation schemes: bounce back (BB), multireflection (MR), linear interpolation (LI), quadratic interpolation (QI), and equilibrium interpolation (EI).

		0°	45°
BB	$0<p\leqslant1$	$\left(\frac{1}{2}-p\right)\left[H-\left(\frac{1}{2}-p\right)\right]+\frac{2}{3}w-\frac{1}{4}$	$\frac{1}{2}\left(\frac{1}{2}-p\right)\left[\sqrt{2}H-\left(\frac{1}{2}-p\right)\right]+\frac{1}{6}w-\frac{1}{8}$
MR	$0<p\leqslant1$	$\frac{2}{3}w$	$\frac{1}{6}w$
LI	$0<p\leqslant\frac{1}{2}$	$\left(\frac{1}{2}-p\right)\left[2\tau-\left(\frac{1}{2}-p\right)\right]+\frac{2}{3}w-\frac{1}{4}$	$\frac{1}{2}\left(\frac{1}{2}-p\right)\left[2\tau-\left(\frac{1}{2}-p\right)\right]+\frac{1}{6}w-\frac{1}{8}$
	$\frac{1}{2}<p\leqslant1$	$\left(p-\frac{1}{2}\right)\left[2\tau-\left(p-\frac{1}{2}\right)-2\right]+\frac{2}{3}w-\frac{1}{4}$	$\frac{1}{2}\left(p-\frac{1}{2}\right)\left[2\tau-\left(p+\frac{3}{2}\right)\right]+\frac{1}{6}w-\frac{1}{8}$
QI	$0<p\leqslant\frac{1}{2}$	$\left(\frac{1}{2}-p\right)\left[2\tau+\left(\frac{1}{2}-p\right)-1\right]+\frac{2}{3}w-\frac{1}{4}$	$\frac{1}{2}\left(\frac{1}{2}-p\right)\left[2\tau+\left(\frac{1}{2}-p\right)-1\right]+\frac{1}{6}w-\frac{1}{8}$
	$\frac{1}{2}<p\leqslant1$	$\left(p-\frac{1}{2}\right)\left[2\tau+\left(p-\frac{1}{2}\right)-1\right]+\frac{2}{3}w-\frac{1}{4}$	$\frac{1}{2}\left(p-\frac{1}{2}\right)\left[2\tau+\left(p-\frac{1}{2}\right)-1\right]+\frac{1}{6}w-\frac{1}{8}$
EI	$0<p\leqslant\frac{1}{2}$	$\left(\frac{1}{2}-p\right)\left(\frac{3}{2}+p\right)+\frac{2}{3}w-\frac{1}{4}$	$\frac{1}{2}\left(\frac{1}{2}-p\right)\left(\frac{3}{2}+p\right)+\frac{1}{6}w-\frac{1}{8}$
	$\frac{1}{2}<p\leqslant1$	$-p\left(p-\frac{1}{2}\right)+\frac{2}{3}w-\frac{1}{4}$	$-\frac{p}{2}\left(p-\frac{1}{2}\right)+\frac{1}{6}w-\frac{1}{8}$

of height L, consisting of H grid cells. The walls are assumed to be symmetrically placed at a distance $p\Delta$ from the nearest fluid node, such that $L=(H+2p-1)\Delta$. When the walls are located midway between grid points, L reduces to $H\Delta$. In a channel flow driven by a body-force density f, the calculated velocity field differs from the exact velocity field

$$u=\frac{f}{2\eta}x(L-x) \tag{22}$$

by a constant slip velocity Δu. We introduce a dimensionless parameter, $\alpha=2\eta\Delta u/f$, such that the normalized slip velocity, $\Delta u/u_{max}$, can then be written as $4\alpha\Delta^2/L^2$, where $u_{max}=u(L/2)=fL^2/8\eta$. Thus, if α grows linearly with H or L, then the boundary condition is first-order accurate, whereas if α is independent of H, then it is second-order accurate. Note that L and $H\Delta$ are the same to first order in H. We have determined the dependence of α on the parameters H, p, τ, and w from a sequence of numerical simulations, using the MRT collision operator described in Sec. III B.

The slip velocities reported in Table II show that the interpolation methods are all second-order accurate, while the BB rule is only first order. However, on average the BB rule is also second-order accurate since terms proportional to H vanish on averaging over all possible wall locations. This explains how the BB rule can exhibit second-order accuracy in a number of practical applications. The LI and QI rules are both second order, but the boundary location depends on fluid viscosity. Since the τ-dependent terms also depend on p this additional slip velocity cannot be tuned away, nor does it vanish on averaging over different boundary locations. For viscous fluids, with $\tau\gg1$, the BB rule, in conjunction with a tuned MRT collision operator, can be more accurate than the LI or QI rules. It is noteworthy that the EI rule is both second order and independent of τ, because it is the interpolation of the nonequilibrium distribution that causes the dependence on fluid viscosity. The multireflection rule leads to boundary conditions that are independent of τ and p. However, even the MR rule is only exact for a specific orientation, unless the tuning parameter is varied for each new angle.

An important question is whether the interpolated boundary rules are second-order accurate for more complex geometries. Therefore, we also simulated a planar Poiseuille flow in a channel oriented at $\tan^{-1}(1/2)$ to the underlying lattice. In this case the slip velocity is no longer constant across the channel [27]; we report values measured at the center of the channel where the slip velocity is largest. In Fig. 3 we show the dependence of the slip velocity on the tuning parameter, w, using a relaxation time $\tau=1/2$. The optimal w was chosen to minimize the deviation near the end points, $p=0.1$ and 0.9, where the errors tend to be the largest. The selected w is
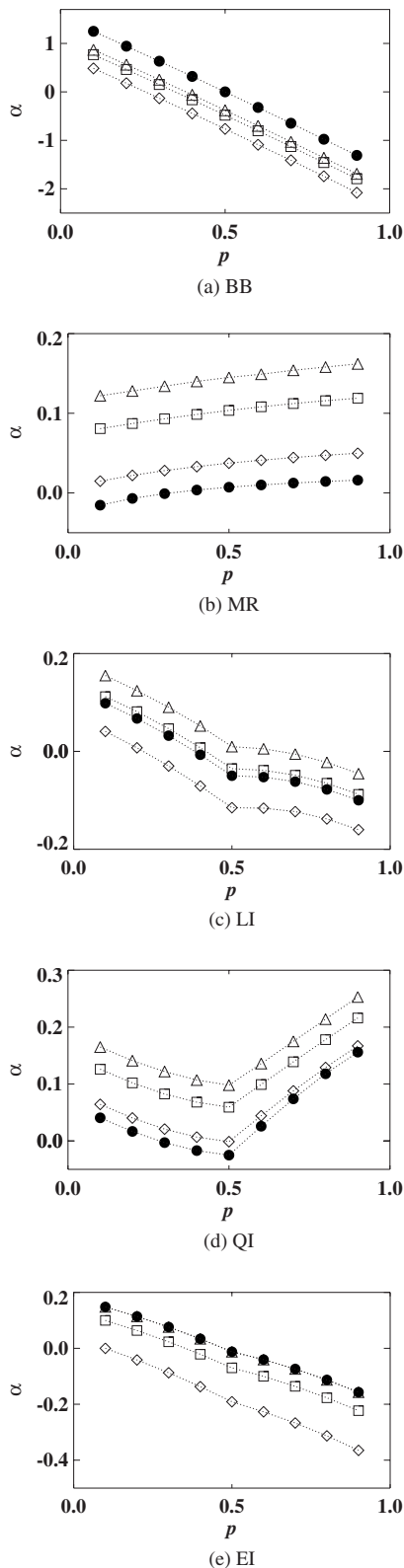
(a) BB

(b) MR

(c) LI

(d) QI

(e) EI

FIG. 3. Effect of variations in the tuning parameter, w, on the dimensionless slip velocity, α, at the center of a $\tan^{-1}(1/2)$ channel. The channel width $L=(16/\sqrt{5}+2p-1)\Delta$ and $\tau=1/2$; results are shown for $w=1/2$ (triangle), $w=3/8$ (square), $w=1/6$ (diamond), and the optimal w (solid circle). The optimal w for each rule is selected to minimize the error at $p=0.1$ and $p=0.9$; $w=17/14$ (BB), $w=3/46$ (MR), $w=1/3$ (LI), $w=1/12$ (QI), $w=1/2$ (EI).

(a) $p = 0.1$

(b) $p = 0.9$
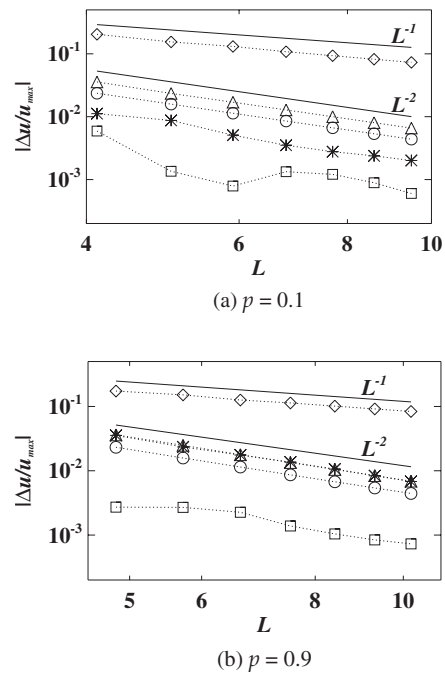
FIG. 4. Resolution dependence of the slip velocity, $|\Delta u/u_{max}|$, at the center of a $\tan^{-1}(1/2)$ channel. The optimal w is used with each rule; BB (diamond), LI (circle), QI (asterisk), MR (square), EI (triangle).

independent of spatial resolution except for very coarse grids. Generally, the no-slip wall moves closer to the solid nodes as w increases, and as a result, the fluid velocity increases with w.

Figure 4 shows the actual slip velocity $\Delta u/u_{max}$ as a function of grid resolution; the optimal value of w was used for each boundary rule. The results are qualitatively similar to those of the 0° and 45° channels. All methods are second-order accurate except the BB rule, which is only second-order accurate on average. Note that for the BB, LI, and EI rules, the slip velocity changes sign between $p=0.1$ and $p=0.9$. Finally, the viscosity dependence of the slip velocity, shown in Fig. 5, is similar to the 0° and 45° channels; the slip velocity is linearly dependent on τ with LI and QI rules, and independent of τ with BB, MR, and EI rules.

In summary, the equilibrium interpolation rule proposed in this paper results in comparable accuracy to the LI and QI rules [26] at low viscosity, with the added advantage that the location of the boundary is independent of fluid viscosity. The ability to simulate accurate flow fields with large viscosities can lead to orders of magnitude reduction in computer time in low-Reynolds number flows. The EI rule is less accurate than the multireflection rule [30], but it only requires a single grid point in the gap between the solid surfaces, whereas the MR rule requires three. Next we examine these same boundary rules in geometries more typical of suspensions and porous media.

B. Flows through cubic arrays of spheres

In order to test the accuracy of the different boundary rules in more realistic geometries, we examined steady
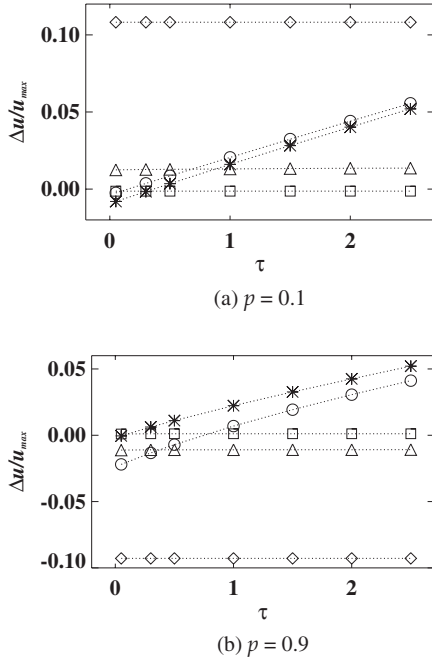
FIG. 5. Viscosity dependence of the slip velocity, $\Delta u/u_{max}$, at the center of a $\tan^{-1}(1/2)$ channel. The channel width $L = (16/\sqrt{5} + 2p - 1)\Delta$. The optimal w is used with each rule; BB (diamond), LI (circle), QI (asterisk), MR (square), EI (triangle).

Stokes flow through simple-cubic and body-centered-cubic arrays of spheres. We calculated the dimensionless permeability, $Q = 6\pi\eta a\langle u\rangle/F$, where $\langle \mathbf{u}\rangle$ is the volume-average velocity of the fluid; the results for Q can be compared with precise values from independent methods [44,45] over a wide range of volume fractions. We used reduced volume fractions, $\chi = (\phi/\phi_{max})^{1/3}$, between 0.4 and 0.95, where $\phi_{max} = \pi/6$ for simple-cubic (SC) arrays and $\phi_{max} = \sqrt{3}\pi/8$ for body-centered-cubic (BCC) arrays. The parameter χ is therefore a measure of the linear expansion of the lattice; the minimum gap between the solid surfaces is given by $2a(1 - \chi)/\chi$, where a is the sphere radius. At the lower volume fractions we use an analytic representation of the permeability [44], but at $\chi = 0.95$ we used an interpolation between numerically calculated data [45]. It is noticeable that the analytic solution [44] deviates from the numerical results in Refs. [44,45] for $\chi > 0.9$; the numerical results are similar even at high volume fractions.

Porous media were constructed from cubic arrays of spheres positioned randomly with respect to the underlying grid. Twenty sets of positions were generated with the same macroscopic configuration, which enables us to measure both the mean and standard deviation of Q. The Reynolds number was identically zero in these simulations due to the choice of equilibrium distribution [Eq. (2)], and the drag force on the spheres is independent of flow direction. The average fluid velocity is calculated by volume, averaging the momentum density of the fluid, $\rho\langle\mathbf{u}\rangle = \langle\mathbf{j}\rangle = N^{-1}\Sigma_{j=1}^{N}\mathbf{j}(\mathbf{r}_j)$, where the sum includes all N nodes in the system. The error in permeability $|Q/Q^* - 1|$ was determined from the computed permeability Q and the independent value, Q^*, from Refs. [44,45].

The optimal tuning parameter for channel flows was found to depend on the channel orientation with respect to the underlying grid. We therefore begin by determining the optimal value of w for a dilute simple-cubic array of spheres ($\chi = 0.4$). Figure 6 shows the error in the permeability for different values of w. The results for all boundary rules are second-order accurate, including the BB rule with a suitable choice of w. The spherical geometry samples different locations and orientations of the boundary and the first-order error is then small. Considering both the overall accuracy and the rate of convergence of the results, we choose the following "optimal" values w for each rule; BB $w = 3/4$, LI $w = 1/6$, QI $w = 1/6$, MR $w = 1/6$, and EI $w = 3/10$, which are then used in the rest of the work. This process resembles the tuning of the hydrodynamic radius proposed previously [4,35] in the context of the bounce-back rule. The present tuning is superior in that the hydrodynamic boundary is now coincident with the mechanical boundary, and, for the MR and EI rules at least, viscosity independent.

The exact mapping of the boundary nodes onto the lattice Boltzmann grid varies with the location of the center of mass of the particle. This produces variations in the flow field around the sphere which can lead to substantial variations in permeability. The error bars in Fig. 7 indicate the maximum and minimum values of the permeability across a simulation set. The bounce-back rule shows the largest fluctuations in permeability as would be expected, but the EI rule shows much smaller variations ($\sim 50\%$) than LI or QI; the multireflection rule has even smaller fluctuations. Figure 7 also shows the viscosity dependence of the permeability. As with channel flows, the permeability obtained with BB, MR, and EI rules are independent of τ, while with LI and QI rules the error in permeability grows in proportion to τ. We note by comparing Figs. 7(a) and 7(b) that the fluctuations in permeability decay rapidly with increasing resolution. The data shown in Fig. 8 indicate that the position-dependent fluctuations in force decay quadratically with increasing grid resolution. Quadratic interpolation shows larger fluctuations than even the bounce-back rule in this case, due to the large τ and the relatively small volume fraction.

The permeability of dilute ($\chi = 0.4$) and dense ($\chi = 0.95$) arrays of spheres was calculated for different grid resolutions, with both simple-cubic and body-centered-cubic structures. We used the optimal value of w for each rule, determined from the permeability of dilute simple-cubic arrays (Fig. 6). In the dilute case ($\chi = 0.4$) there are always at least three fluid nodes in the gap between particle surfaces, but in the dense case ($\chi = 0.95$) there is typically only one fluid node in the gap. If there are insufficient fluid nodes for the interpolation rule, we reduce the MR and QI rules to the LI rule, and the LI rule to the BB rule, depending on the number of available nodes. The EI rule can always be applied in one of its interpolated forms unless the gap between the surfaces is less than Δ; in this case we use the BB rule. The proposed mixed methods are stable, and the implementation is summarized in Table III.

Figure 9 illustrates the convergence of the permeability for different geometries, different packing fractions, and different fluid viscosities. In the dilute packings [Figs. 9(a),
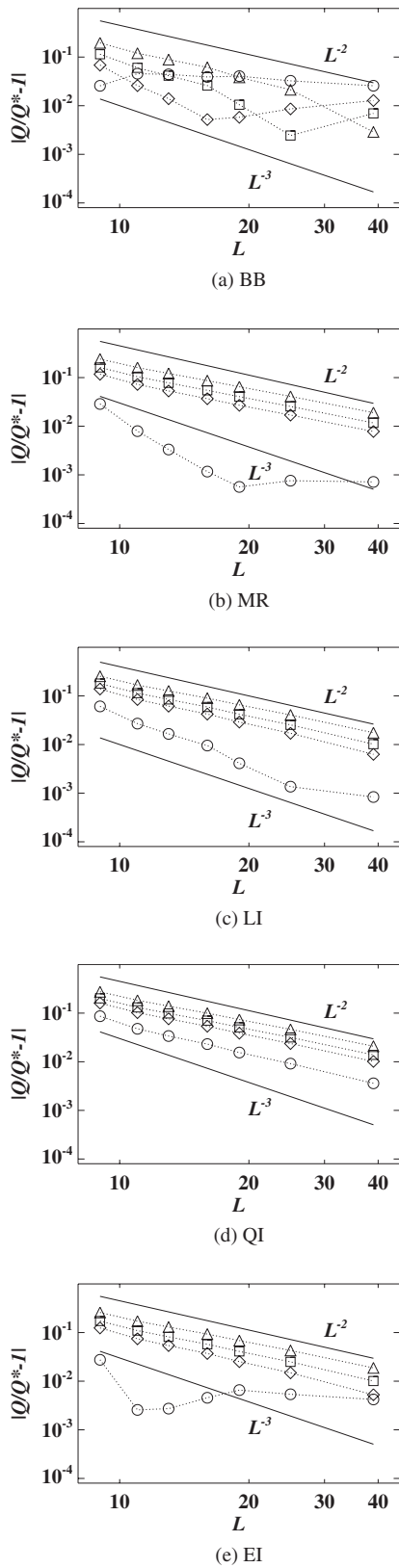
(a) BB

(b) MR

(c) LI

(d) QI

(e) EI

FIG. 6. Error in the permeability $|Q/Q^*-1|$ for a simple-cubic array of spheres as a function of grid resolution. L is the number of grid points spanning the periodic unit cell, $\chi=0.4$ and $\tau=1/2$. Results are shown for $w=3/4$ (triangle), $w=1/2$ (square), $w=3/8$ (diamond), and $w=1/6$ (circle).
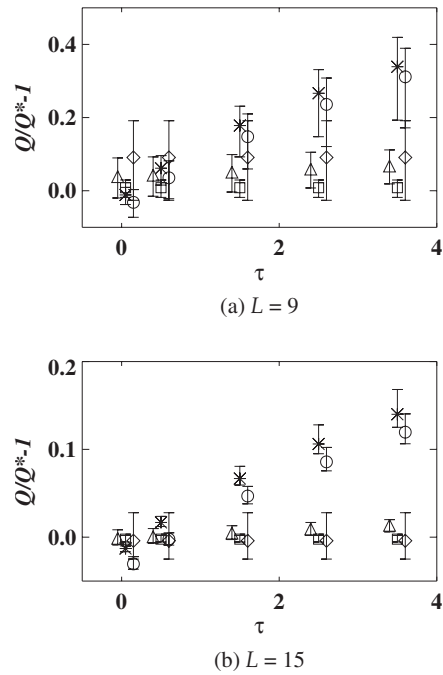

(a) $L = 9$

(b) $L = 15$

FIG. 7. Viscosity dependence of the error in permeability for a simple-cubic array of spheres ($\chi=0.6$). Results are shown for relaxation times $\tau=0.05, 0.5, 1.5, 2.5, 3.5$. For clarity the results are plotted with small offsets from the actual values of τ. The error bars denote the maximum and the minimum values in the simulation sets; BB (diamond), LI (circle), QI (asterisk), MR (square), EI (triangle).

9(c), and 9(e)], all the rules are second-order accurate. In general, the MR rule has the lowest error, by up to an order of magnitude, while EI is slightly less accurate than LI and QI at low viscosity [Fig. 9(a)] but more accurate at higher viscosity [Figs. 9(c) and Fig. 9(e)]. In fact, at the higher viscosity ($\tau=1.5$), the bounce-back rule tends to be at least as accurate as the LI or QI rules.

For dense packings [Figs. 9(b), 9(d), and 9(f)], the errors are typically an order of magnitude larger than in the dilute case when the particle size is kept constant. But for the same fluid volume, L^3, the errors are quite similar. This gives a
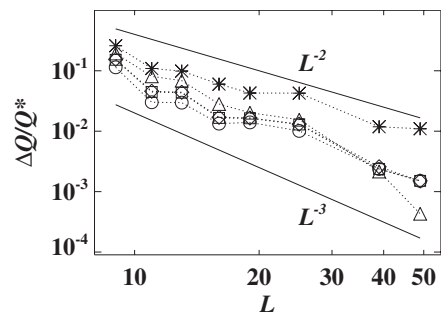

FIG. 8. Grid-dependent fluctuations in permeability $\Delta Q/Q^*$ for a simple-cubic array of spheres ($\tau=3/2$, $\chi=0.4$). The difference between the maximum and minimum permeability for different locations of the sphere are shown as a function of grid resolution; BB (diamond), LI (circle), QI (asterisk), MR (square), EI (triangle).

TABLE III. Mixed interpolation rules. The LI, QI, and MR interpolations require additional neighboring nodes, whereas the EI rule does not. However the EI rule does have the additional restriction that the gap between the solid surfaces must be greater than one grid spacing.

Available fluid nodes	Boundary rules				
$\geqslant 3$	BB	MR	QI	LI	EI
2	BB	LI	LI	LI	EI
1	BB	BB	BB	BB	EI

useful empirical rule for predicting the accuracy of LBE simulations at different solids loadings. For comparable relative error, the fluid volume per particle should be similar, independent of the volume fraction. Note that for the BCC packing, the volume per particle is $L^3/2$, because there are two particles in the unit cell. In dense simple-cubic packings the EI rule is quite comparable to the MR rule and is more accurate than either LI or QI, especially at the higher viscosity. However, in BCC packing the MR rule is more accurate than EI. Once again the accuracy of the LI and QI rules is degraded at larger viscosities.

C. Mass leakage

A drawback of these interpolation methods is that the total fluid mass is not conserved. In special cases, such as a chan-nel flow with the walls symmetrically placed on the grid, there is no mass leakage; the gain and loss of mass from the interpolations are exactly canceled by each other. However, in general, solid surfaces are not located in symmetric positions, so that the fluid mass tends to keep increasing or decreasing over time, depending on the position of the boundaries. In a dynamical simulation some procedure to compensate for variations in fluid mass is necessary. Mass conserving interpolations have been developed [46,47] but they are more complicated to implement and do not give second-order accuracy in general.

The mass leakage per time step, $\Delta M = \Sigma_j [\rho(\mathbf{r}_j,t) - \rho^{eq}]/t$, is roughly constant for a given configuration and proportional to the average velocity of fluid. The results in Fig. 10 show that $\Delta M/\langle u \rangle$ is close to viscosity independent with MR

(a) Simple Cubic: $\chi = 0.40$, $\tau = 0.05$

(b) Simple Cubic: $\chi = 0.95$, $\tau = 0.05$

(c) Simple Cubic: $\chi = 0.40$, $\tau = 1.5$

(d) Simple Cubic: $\chi = 0.95$, $\tau = 1.5$

(e) Body-Centered Cubic: $\chi = 0.40$, $\tau = 1.5$
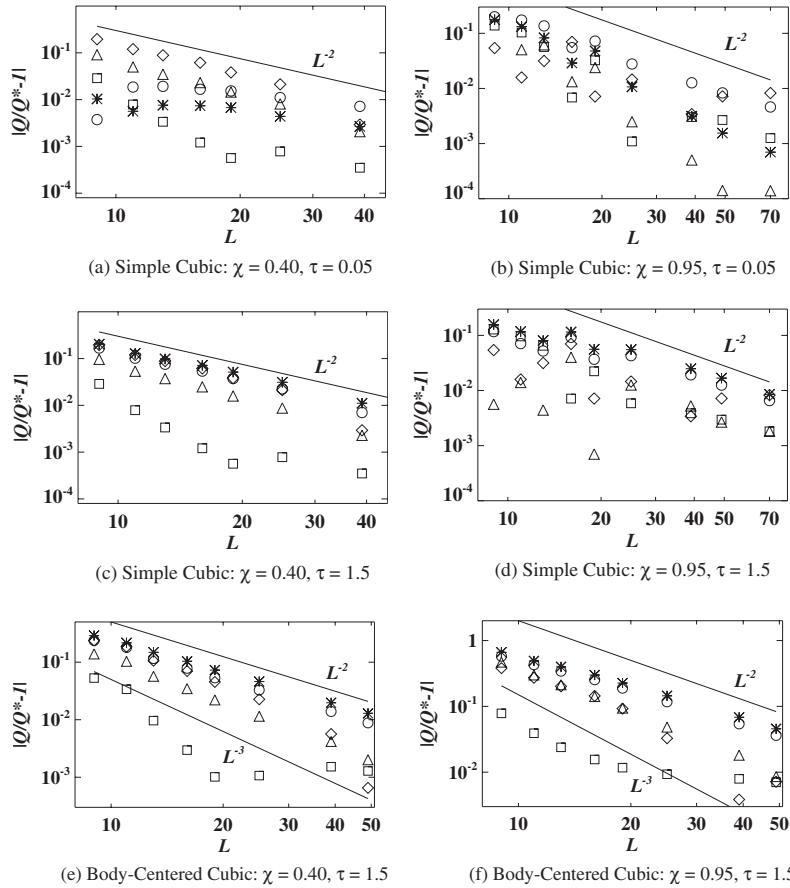
(f) Body-Centered Cubic: $\chi = 0.95$, $\tau = 1.5$

FIG. 9. Error in the permeability $|Q/Q^* - 1|$ for simple-cubic and body-centered-cubic array of spheres as a function of grid resolution. Results are shown for different solid packing fractions and fluid viscosity; BB (diamond), LI (circle), QI (asterisk), MR (square), EI (triangle).
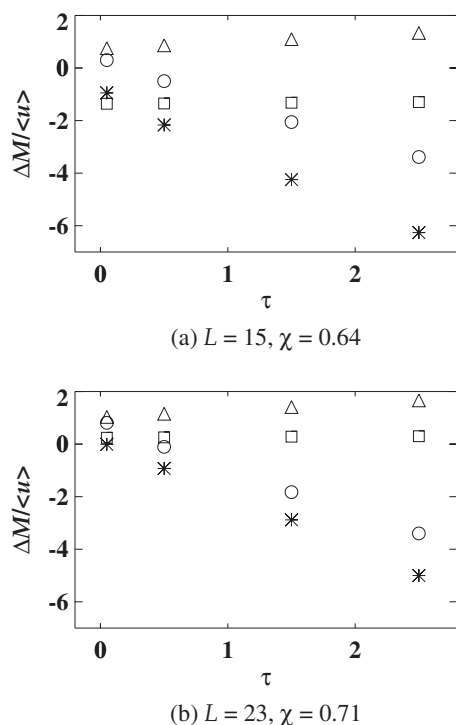
(a) $L = 15, \chi = 0.64$

(b) $L = 23, \chi = 0.71$

FIG. 10. Viscosity dependence of the mass leakage in a simple-cubic array of spheres. Results are shown for two different size spheres $a = 4.8$ and $a = 8.2$; LI (circle), QI (asterisk), MR (square), EI (triangle).

and EI rules, while with LI and QI it linearly increases with τ. LI and QI rules have the largest mass leakage, while EI and MR are smaller, particularly at large τ. However, even though the mass gain or loss increases with time, we did not observe any variation in the fluid velocity. We conclude that in the incompressible limit the mass leakage does not affect the velocity field [3].

V. CONCLUSIONS

We have proposed an interpolation method for implementing a no-slip boundary condition in lattice Boltzmann simulations. By interpolating only the equilibrium portion of the distribution, second-order accuracy is maintained but the number of fluid nodes needed is reduced; instead information about the equilibrium distribution on the boundary surface is used for the interpolation. The EI rule can be used with only a single fluid node, as long as the gap between surfaces is larger than Δ.

The accuracy of several different boundary rules was evaluated for flows in inclined channels and flows though porous media composed of regular arrays of spheres. We used a multiple-relaxation time LBE model, but with a different set of eigenvectors from Refs. [30,32]. The alternate set of "weighted" eigenvectors [31] does not project the equilibrium distribution onto the kinetic modes. We have used a two-relaxation-time model, with a single tuning parameter, w, to control the location of the no-slip boundary.

The convergence of all the interpolation methods is second order, in contrast to the first-order accuracy typical of the BB rule. However, in more complex geometries such as arrays of spheres, the bounce-back rule is also second order, because the first-order terms tend to average out when a number of different positions and orientations are sampled. In general the MR rule is most accurate and independent of viscosity. The the LI and QI rules are second-order accurate but viscosity dependent. They show a significant improvement in accuracy compared with the BB rule at lower viscosity ($\tau \lesssim 1$), but not in more viscous fluids. The EI rule is independent of viscosity, and has significantly better accuracy for highly viscous flows. Our results suggest that the EI rule is especially suitable for flows through small gaps because it can maintain second-order accuracy down to the level of a single grid spacing.

ACKNOWLEDGMENTS

[1] F. M. Auzerais, J. Dunsmuir, B. B. Ferréol, N. Martys, J. Olson, T. S. Ramakrishnan, D. H. Rothman, and L. M. Schwartz, Geophys. Res. Lett. **23**, 705 (1996).

[2] A. Koponen, D. Kandhai, E. Hellen, M. Alava, A. Hoekstra, M. Kataja, K. Niskanen, P. Sloot, and J. Timonen, Phys. Rev. Lett. **80**, 716 (1988).

[3] C. Pan, L. S. Luo, and C. T. Miller, Comput. Fluids **35**, 898 (2006).

[4] A. J. C. Ladd, J. Fluid Mech. **271**, 311 (1994).

[5] C. K. Aidun, Y. N. Lu, and E. Ding, J. Fluid Mech. **373**, 287 (1998).

[6] A. J. C. Ladd, Phys. Rev. Lett. **88**, 048301 (2002).

[7] N.-Q. Nguyen and A. J. C. Ladd, J. Fluid Mech. **525**, 73 (2005).

[8] P. Ahlrichs and B. Dünweg, J. Chem. Phys. **111**, 8225 (1999).

[9] O. B. Usta, A. J. C. Ladd, and J. E. Butler, J. Chem. Phys. **122**, 094902 (2005).

[10] O. Kuksenok, J. M. Yeomans, and A. C. Balazs, Phys. Fluids **6**, 108 (1994).

[11] O. B. Usta, J. E. Butler, and A. J. C. Ladd, Phys. Fluids **18**, 031703 (2006).

[12] A. J. C. Ladd, J. Fluid Mech. **271**, 285 (1994).

[13] R. Cornubert, D. d'Humières, and C. D. Levermore, Physica D **47**, 241 (1991).

[14] I. Ginzburg and P. M. Adler, J. Phys. II **4**, 191 (1994).

[15] D. P. Ziegler, J. Stat. Phys. **71**, 1171 (1993).

[16] P. A. Skordos, Phys. Rev. E **48**, 4823 (1993).

[17] D. R. Noble, S. Y. Chen, J. G. Georgiadis, and R. O. Buckius,

Phys. Fluids **7**, 203 (1995).

[18] T. Inamuro, M. Yoshino, and F. Ogino, Phys. Fluids **7**, 2928 (1995).

[19] I. Ginzburg and D. d'Humières, J. Stat. Phys. **84**, 927 (1996).

[20] M. Junk and Z. Yang, Phys. Rev. E **72**, 066701 (2005).

[21] A. J. C. Ladd and D. Frenkel, Phys. Fluids A **2**, 1921 (1990).

[22] O. Filippova and D. Hänel, J. Comput. Phys. **147**, 219 (1998).

[23] S. Chen and G. D. Doolen, in *Annual Review of Fluid Mechanics*, edited by J. L. Lumley, M. V. Dyke, and H. L. Reed (Annual Reviews Inc., Palo Alto, CA, 1998), Vol. 30, pp. 329–364.

[24] R. W. Mei, L. S. Luo, and W. Shyy, J. Comput. Phys. **155**, 307 (1999).

[25] R. Verberg and A. J. C. Ladd, Phys. Rev. E **65**, 016701 (2001).

[26] M. Bouzidi, M. Firdaouss, and P. Lallemand, Phys. Fluids **13**, 3452 (2001).

[27] M. Rohde, D. Kandhai, J. J. Derksen, and H. E. A. Van den Akker, Phys. Rev. E **67**, 066703 (2003).

[28] D. Z. Yu, R. W. Mei, L. S. Luo, and W. Shyy, Prog. Aerosp. Sci. **39**, 329 (2003).

[29] P. Lallemand and L. S. Luo, J. Comput. Phys. **184**, 406 (2003).

[30] I. Ginzburg and D. d'Humières, Phys. Rev. E **68**, 066614 (2003).

[31] R. Adhikari, K. Stratford, M. E. Cates, and A. J. Wagner, Europhys. Lett. **3**, 473 (2005).

[32] D. D'Humieres, I. Ginzburg, M. Kraftzyck, P. Lallemand, and

L. S. Luo, Proc. R. Soc. London, Ser. A **360**, 437 (2002).

[33] F. Higuera, S. Succi, and R. Benzi, Europhys. Lett. **9**, 345 (1989).

[34] F. J. Higuera and J. Jimenez, Europhys. Lett. **9**, 663 (1989).

[35] A. J. C. Ladd and R. Verberg, J. Stat. Phys. **104**, 1191 (2001).

[36] H. Chen, S. Chen, and W. H. Matthaeus, Phys. Rev. A **45**, R5339 (1992).

[37] Y. H. Qian, D. d'Humières, and P. Lallemand, Europhys. Lett. **17**, 479 (1992).

[38] D. D'Humieres, Prog. Astronaut. Aeronaut. **159**, 450 (1992).

[39] P. Lallemand and L. S. Luo, Phys. Rev. E **61**, 6546 (2000).

[40] G. R. McNamara and B. J. Alder, in *Microscopic Simulations of Complex Hydrodynamic Phenomena*, edited by M. Mareschal and B. L. Holian (Plenum, New York, 1992).

[41] U. Frisch, D. d'Humières, B. Hasslacher, P. Lallemand, Y. Pomeau, and J.-P. Rivet, Complex Syst. **1**, 649 (1987).

[42] G. R. McNamara and B. J. Alder, Physica A **194**, 218 (1993).

[43] P. J. Dellar, J. Comput. Phys. **190**, 351 (2003).

[44] A. S. Sangani and A. Acrivos, Int. J. Multiphase Flow **8**, 193 (1982).

[45] A. A. Zick and G. M. Homsy, J. Fluid Mech. **115**, 13 (1982).

[46] R. Verberg and A. J. C. Ladd, Phys. Rev. Lett. **84**, 2148 (2000).

[47] M. Rohde, J. J. Derksen, and H. E. A. Van den Akker, Phys. Rev. E **65**, 056701 (2002).

[48] There is a typographical error in Table II of Ref. [30]. In the column UQI the parameter κ_1 should be $\delta_q(1+2\delta_q)$.